Case Studies in Construction Materials 23 (2025) e05175

Contents lists available at ScienceDirect

Case Studies in Construction Materials

journal homepage: www.elsevier.com/locate/cscm

Case study

Design of solid waste-based superfine tailings cemented paste backfill based on machine learning and MAA model

Yafei Hu [a], Ruipeng Hu [a], Lujing Zheng [b], Bin Han [a,*], Zhiyi Liu [c], Sitao Zhu [a,*]

[a] School of Civil and Resource Engineering, University of Science and Technology Beijing, Beijing 100083, China
[b] Guizhou Jinfeng Mining Limited, Guizhou 562204, China
[c] School of Mining Engineering, North China University of Science and Technology, Tangshan 063200, China

ARTICLE INFO

Keywords:
Green filling
Superfine tailings
Machine learning
Solid waste
Mix proportion design

ABSTRACT

The application of solid waste in filling mining has become an essential direction for developing green mines. This study prepared mixed aggregates using superfine tailings (ST), fly ash (FA), and silica fume (SF), and developed a solid waste-based superfine tailings cemented paste backfill (SCPB) by using steel slag (SS), granulated blast furnace slag (GBFS), and desulfurization gypsum (FDG) as binder. The modified Andreasen-Andersen (MAA) model was used to optimize the proportion of mixed aggregates. Response surface method (RSM) experiments were conducted to investigate the development of the compressive strength of SCPB. Various microscopic testing methods were employed to reveal its hydration mechanism, and a machine learning method was used to construct an optimization model for the mix proportion of SCPB. The results indicate that the residual sum of squares (RSS) decreases with increasing ST dosage. When SF, FA, and ST are mixed in a mass ratio of 10:20:70, i.e., m(SF):m(FA):m(ST) = 10:20:70, RSS reaches a minimum RSS of 153.07, at which the mixed aggregate exhibits the lowest packing density. The compressive strength of SCPB increases with the addition of binder and slurry concentration at all curing times, and first increases then decreases with the increase of SF dosage. SS, GBFS, and FDG interact to form ettringite (AFt) and calcium silicate hydrate (C-S-H) and other hydration products, which are the fundamental source of SCPB strength. Additionally, the intelligent filling mix proportion design model developed in this study, which integrates the Sparrow Search Algorithm (SSA), Extreme Learning Machine (ELM), and Genetic Algorithm (GA), can rapidly and accurately obtain the optimal backfill mix proportion under actual engineering constraints, with an accuracy of over 90 %. The relevant research provides methodological guidance for the efficient recycling and utilization of solid waste materials, as well as the efficient application of cemented filling technology.

1. Introduction

Cemented paste backfill mining technology involves mixing tailings generated during mineral processing with cement-based binder to prepare backfilling materials, which are then injected into abandoned mine voids [1–3]. This technology enhances mining safety while effectively addressing ground subsidence and environmental pollution issues, aligning with the development direction of green mining. However, as mineral processing technology continues to mature, tailings particles are becoming increasingly fine and forming

* Corresponding authors.
E-mail addresses: bin.han@ustb.edu.cn (B. Han), zhusitao@ustb.edu.cn (S. Zhu).

https://doi.org/10.1016/j.cscm.2025.e05175
Received 23 May 2025; Received in revised form 30 July 2025; Accepted 12 August 2025
Available online 13 August 2025
2214-5095/© 2025 The Authors. Published by Elsevier Ltd. This is an open access article under the CC BY-NC license (http://creativecommons.org/licenses/by-nc/4.0/).

superfine tailings(ST), which reduces the strength of cemented backfill materials using tailings as aggregate, leading to mine safety issues [4–6]. Meanwhile, cement, as the main binder, is expensive, and its production process is accompanied by high pollution and high carbon emissions, which not only increases the cost of backfilling but also fails to align with the current global concept of clean and low-carbon production [7–9]. Therefore, under the premise of ensuring the strength of the backfill, improving the utilization rate of superfine tailings and developing low-carbon binders that can replace cement have become urgent issues in the field of backfilling mining.

Superfine tailings have fine particle sizes, poor dispersibility, and low filling strength. To solve these issues, scholars have conducted extensive research. Based on the strength test data of superfine tailings cemented backfilling materials, Fu et al.[10] proposed using the limiting volume concentration to characterize the group properties of materials, starting from the microstructure of the filling slurry. Combining the relationship between the water-cement ratio and strength in the experiment, they constructed a three-variable strength calculation model, providing a basis for the design of the proportion of superfine tailings backfilling slurry. Rao et al.[11] conducted in-depth research on the application of fly ash as an admixture in tailings backfilling, clarified the mechanism of fly ash in enhancing the strength of tailings backfill, and discovered the unique advantages of fly ash in tailings backfilling. Li et al.[12] used superfine tailings as backfill aggregate and used coal slag to replace part of the cement-based materials to reduce backfilling costs while keeping the strength properties of the cemented tailings backfill. The study showed that the addition of coal slag can improve the slurry fluidity and backfill strength, and effectively reduce the amount of cement used and solid waste emissions. Zou et al.[13] improved the strength and ductility of superfine tailings cemented paste backfill through the synergistic use of polypropylene fibers and silica fume, providing an effective method for the recycling of superfine tailings.

The above research has conducted useful explorations into the recycling of superfine tailings and proven their application potential, but the high costs and environmental problems associated with the use of cement as a cementitious material still remain. Tian et al.[14] conducted a study on the optimal mix proportion of all-solid waste cemented paste backfill materials using the response surface method, finding that the water-to-cement ratio had the most significant effect on the performance of the backfill materials. The optimal mix proportion was determined to be a water-to-cement ratio of 0.39, water glass modulus of 1.38, and alkali equivalent of 4.7 %, and the effectiveness of the response surface method in optimizing the mix proportion was verified. Yang et al.[15] prepared solid waste-based binder using industrial solid wastes such as steel slag, blast furnace slag, and desulfurization gypsum, studied their application in low-carbon concrete, and demonstrated the feasibility of all-solid waste low-carbon concrete filling. Hu et al.[16] proposed a cement-solid waste composite binder system and optimized the mix ratio of tailings wet shotcrete using the response surface method and intelligent model, proving that the composite binder system can effectively improve concrete strength.

Currently, there is little research on solid waste-based binders and backfilling materials, especially those using superfine tailings as aggregates. Furthermore, research on the optimization of their filling proportions and strength formation mechanisms is still immature. Meanwhile, solid waste materials such as fly ash and silica fume are rich in silicate components. These active minerals not only optimize aggregate gradation but also effectively promote hydration reactions, thereby significantly improving the strength and stability of the backfilling material. For example, Wen et al.[17] used fly ash and silica fume as admixtures and guided the optimization of particle gradation for ultra-high-performance concrete (UHPC) using the modified Andreasen-Andersen (MAA) model. They found that when the silica fume content was high, the bulk density of UHPC could be significantly improved. They further found that fly ash and silica fume react in an alkaline environment to form more gel, which improves the density and compressive strength of UHPC materials. Therefore, the use of these active minerals to prepare superfine tailings fillers also has high research value.

Machine learning is increasingly being applied in the field of backfill mining, enhancing the efficiency and safety of mining operations. Particularly in the prediction of backfill material strength, machine learning models combined with optimization algorithms have found widespread application. Hu et al. utilized machine learning models to study the mechanical properties of SCPB, with experimental results indicating that machine learning can effectively predict its strength, providing technical support for the resource utilization of tailings [18]. Semudiamhen et al. combined machine learning with infrared radiation (IR) indicators to improve the prediction accuracy of the unconfined compressive strength (UCS) of backfill materials [19]. Jooshaki et al. discussed the feasibility of machine learning in the utilization of mineralogical data in the mining and mineral industry, identified challenges in data quality and methodological diversity in this field, and pointed the way forward for the intelligent development of the mining industry [20]. Liu et al. pointed out that in open pit mining, machine learning can enhance ore body knowledge by analyzing measurement-while-drilling (MWD) data, which is critical for predicting geological conditions and optimizing mining operations [21]. Shah et al. demonstrated that machine learning technology combined with backfilling techniques using hardened backfill materials can improve mineral recovery rates in potash mining [22]. The above research demonstrates the feasibility of applying machine learning technology in the mining field and provides insights for establishing a backfill strength prediction model based on machine learning in this study.

Based on this, this study uses steel slag(SS), granulated blast furnace slag(GBFS), desulfurization gypsum(FDG) to prepare solid waste-based binder, optimizes the mix design of superfine tailings, silica fume(SF) and fly ash(FA) according to the MAA model, investigates the mechanical properties and hydration mechanism of solid waste-based superfine tailings cemented paste backfill(SCPB) by combining various microstructural characterization methods, and constructs a strength prediction model and proportion optimization model of SCPB based on machine learning methods. The novelty of this study lies in the development of an all-solid-waste binder for superfine tailings backfill and the integration of a modified particle packing model with advanced machine learning for mix proportion optimization. This comprehensive approach has not been reported in previous studies. Specifically, unlike prior works, we utilize industrial wastes (steel slag, blast furnace slag, desulfurization gypsum) as the sole binder components and combine Andreasen-Andersen model-based gradation optimization with a hybrid intelligent algorithm to achieve over 90 % prediction accuracy for backfill strength. These novel contributions advance the methodology and application of green mining backfill.

2. Materials and methods

2.1. Materials

2.1.1. Binder

The three-component composite binder used in this study is prepared from SS, FDG, and GBFS. SS and GBFS are provided by Ansteel Group Corporation in China, while FDG is sourced from a power plant in Northeast China. All raw materials must undergo crushing to activate their hydration activity. After grinding in a ball mill, the specific surface areas of the materials are S_{SS}= 455 m^2/kg, S_{FDG}= 422 m^2/kg, and S_{GBFS}= 335 m^2/kg. The composition of the three raw materials is analyzed by XRF and presented in Table 1. Based on extensive exploratory experiments, the optimal ratio of SS:GBFS:FDG for the solid waste-based binder is 35:40:25.

.

2.1.2. Aggregate

Due to the extremely low strength of the ST-prepared backfilling body, this study prepares a mixed aggregate by combining ST with SF and FA, which possess certain activity. The ST used in the experiment originates from a gold mine in Guizhou Province, SF is sourced from a silicon material production company in Gansu Province, and fly ash is an industrial by-product generated from coal combustion at a power plant in Gansu Province. The XRF analysis results of the 3 aggregates are shown in Table 2. As shown in Table 2, the activity index(CaO%/SiO_2%) of ST and SF is low, with activity rates of 0.031 and 0.005, respectively, indicating that they are inert materials. The main components of FA are SiO_2, Al_2O_3, and CaO, accounting for approximately 92 %, with an activity index of 0.467, indicating potential activity.

2.2. Methods

2.2.1. Aggregate proportion optimization

By scientifically and reasonably improving the particle size distribution to form the most dense packing density of mixed aggregates, the objective of aggregate proportion optimization can be achieved. The MAA model proposed by Dinger and Funk was used to carry out aggregate proportion optimization [23].

$$P(D) = \frac{D^q - D_{\min}^q}{D_{\max}^q - D_{\min}^q} \tag{1}$$

In Eq. (1), D is the particle size, μm; P is the particle content, %; D_{max} is the maximum particle size, μm; D_{min} is the minimum particle size, μm; q is the distribution modulus, whose value depends on the ratio of large particles to fine particles in the system, and the more coarse particles there are, the larger q is.

Using MATLAB software to model the MAA model, the least squares method is employed to adjust the proportion of raw materials in the dry mixture. The deviation between the synthesis curve function of the mixture under different raw material proportions and the target curve function of the MAA model is calculated, and the residual sum of squares (RSS) is used for characterization [24]. The RSS calculation formula is as follows.

$$RSS = \sum_{i=1}^{n} \left(P_{mix}(D_i^{i+1}) - P_{tra}(D_i^{i+1})\right)^2 \tag{2}$$

In Eq. (2), P_{mix} and P_{tra} are the mixed material synthesis curve function and the MAA model target curve function, respectively; n denotes the number of parts into which the function is divided when calculating RSS; i denotes each part when calculating RSS; andD_i^{i+1}denotes the particle size interval of the division.

The cumulative size distribution of aggregate particles is shown in Table 3. From Table 3, D_{max}= 756.45 μm, D_{min}= 0.19 μm. The distribution modulus q= 0.23 is taken to construct the target curve of MAA model as shown in Fig. 1. The optimal grain size curves of mixed aggregates are obtained using the MMA model and shown in Fig. 1, and the deviations between the synthetic curve functions of different mixed aggregates and the target curve functions of the MAA model are analyzed, and 10 sets of results are obtained and shown in Table 4.

2.2.2. Experimental design

To investigate the effects of various factors on the macro strength of SCPB, obtain a backfilling proportion that satisfactorily meets strength requirements, reduce the number of experiments, and improve experimental efficiency, this study employed the response

Table 1
Chemical composition of SS, GBFS, and FDG.

Content	SiO_2	CaO	MgO	Fe_2O_3	Al_2O_3	SO_3	K_2O	MnO
GBFS	28.52 %	40.52 %	7.86 %	2.54 %	13.08 %	1.68 %	0.39 %	0.65 %
SS	21.00 %	37.98 %	8.38 %	18.93 %	6.72 %	0.72 %	0.21 %	3.01 %
FDG	4.87 %	47.84 %	2.19 %	0.80 %	1.27 %	40.22 %	0.35 %	0.05 %

Table 2
Chemical composition of ST, FA, and SF.

Content	SiO_2	CaO	MgO	Fe_2O_3	Al_2O_3	Na_2O	K_2O	other
ST	67.77 %	3.42 %	4.79 %	2.26 %	14.47 %	0.14 %	0.21 %	6.93 %
FA	57.47 %	6.88 %	0.78 %	4.59 %	26.82 %	0.82 %	1.15 %	1.48 %
SF	94.12 %	0.51 %	0.33 %	0.45 %	0.37 %	0.18 %	1.85 %	1.18 %

Table 3
The cumulative size distribution of aggregate particles.

D/μm	P/%		
	SF	FA	ST
0.19	0	0	0.1
0.77	8.9	2.4	5.4
1.45	27.6	3.7	7.9
2.75	48.4	4.5	11.5
5.92	64.0	12.9	19.7
11.21	75.6	34.2	27.9
18.66	87.1	55.4	37.2
35.33	97.8	77.5	57.1
66.89	100.0	95.2	81.2
126.65	100.0	100.0	94.9
756.45	100.0	100.0	100.0

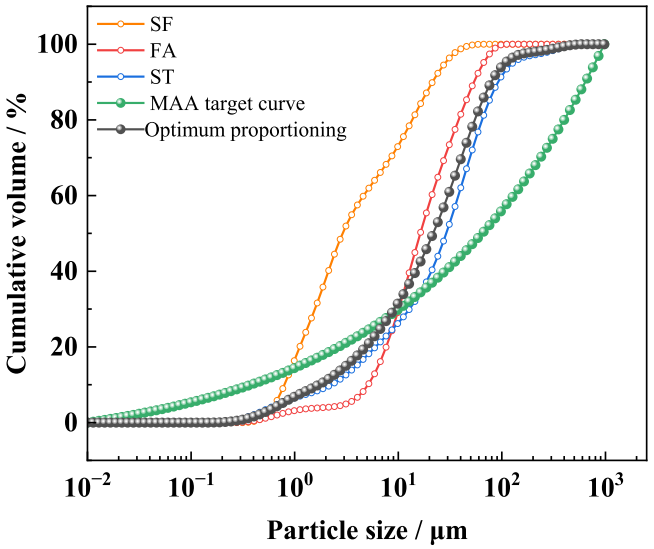

Fig. 1. Particle size distribution curve and target curve of the MAA model.

Table 4
Mixed aggregate proportion based on the MAA model and RSS.

m(SF):m(FA):m(ST)	RSS
10:40:50	163.63
15:35:50	164.55
20:30:50	166.11
10:30:60	158.26
15:25:60	159.16
20:20:60	160.72
10:20:70	153.07
15:15:70	153.94
20:10:70	155.50

surface method(RSM) for experimental design, using Design-Expert 13 software [25,26].

Based on extensive preliminary exploratory experiments, the proportion of fly ash in the aggregate is set at 10 %–20 %. When the slurry concentration is 68 %–76 % and the solid waste-based binder dosage is 6 %–10 %, the fluidity and strength of the SCPB slurry can satisfy the technical requirements. Based on this, this study uses SF dosage, binder dosage, and slurry concentration as independent variables (denoted as X_1, X_2, and X_3, respectively), and the 7d 14d, and 28d uniaxial compressive strength (UCS) of SCPB as response values (denoted as Y_1, Y_2, and Y_3, respectively), to conduct RSM experiments. The specific experimental scheme is shown in Table 5.

2.2.3. Testing methods

(1) UCS. Grind the side of the cured test specimen to a smooth surface and place it centrally in the pressure machine fixture, ensuring that the compressed surface remains parallel to the loading device. Set the loading rate to 1 mm/min. Start the pressure machine to conduct the strength test, and use the average value of the test results from three specimens as the strength result for that specimen. The equipment used is the American HUMBOLDTHM-5030 pressure testing machine, with a maximum loading capacity of 50 kN.

(2) SEM. Prepare SCPB samples with dimensions of 1 cm × 1 cm × 0.5 cm for SEM testing. When the specified curing time is reached, the specimens are immersed in anhydrous ethanol solution for 24 h to halt hydration, then placed in a vacuum drying oven at 40°C to remove residual anhydrous ethanol, and finally undergo gold sputtering treatment. The microstructure of the SCPB is observed using a scanning electron microscope. The equipment used is the VEGA3-type scanning electron microscope manufactured by TESCAN of the Czech Republic.

(3) XRD. The samples are crushed into small pieces no larger than 2 mm, soaked in anhydrous ethanol for 2 h, then dried in a vacuum at 40°C, manually ground into powder, sieved through a 200-mesh standard sieve, and the sieved material is subjected to XRD analysis. The equipment used is the XRD-7000 X-ray diffractometer from Shimadzu Corporation, Japan.

(4) FTIR. The sample is vacuum dried at 40°C for 24 h until all moisture is completely evaporated. The dried sample is ground into a fine powder, passed through a standard 80-mesh sieve, and placed in an FTIR instrument. The chemical structure and functional groups of the sample are detected using a Nicolet iS50 Fourier transform infrared spectrometer from Thermo Fisher Scientific in the United States.

3. Results and discussion

3.1. Experimental results and response model

3.1.1. Experimental results

The RSM experimental results are shown in Table 6.

3.1.2. RSM model

Using Design-Expert 13 software, a multiple regression analysis is performed on the experimental results of 17 groups to construct a quadratic polynomial regression equation for UCS as a function of SF dosage, binder dosage, and slurry concentration, as shown in Eqs. (3) to (5). Fig. 2 presents a comparison between the experimental values and predicted values of UCS calculated based on the regression equation. From Fig. 2, it can be observed that the experimental values and predicted values show a high degree of agreement, indicating that the strength model is effective.

$$Y_1^* = 9.2044 + 0.0204X_1 + 0.1346X_2 - 0.2738X_3 - 0.0016X_1X_2 + 0.0008X_1X_3 + 0.0003X_2X_3 - 0.0023X_1^2 - 0.0058X_2^2 + 0.0019X_3^2 (R^2 = 0.9863) \quad (3)$$

$$Y_2^* = 4.5538 + 0.0053X_1 + 0.3763X_2 - 0.1537X_3 - 0.0016X_1X_2 + 0.0009X_1X_3 - 0.0025X_2X_3 - 0.0019X_1^2 - 0.0085X_2^2 + 0.0012X_3^2 (R^2 = 0.9842) \quad (4)$$

$$Y_3^* = 4.6507 + 0.0691X_1 + 0.6066X_2 - 0.1946X_3 - 0.0041X_1X_2 + 0.0009X_1X_3 - 0.0035X_2X_3 - 0.0034X_1^2 - 0.0144X_2^2 + 0.0015X_3^2 (R^2 = 0.9853) \quad (5)$$

3.1.3. Model verification

To verify the validity of the RSM model, the above quadratic polynomial regression equations are analyzed by ANOVA [27,28], and the results are shown in Table 7. Table 7 shows that the P-value of the significance test of the 3 response models is less than 0.0001

Table 5
Mixed aggregate proportion based on the MAA model and RSS.

Factor	Level code		
	-1	0	1
SF dosage (X_1, %)	10	15	20
Binder dosage (X_2, %)	6	8	10
Slurry concentration (X_3, %)	68	72	76

Table 6
RSM Experimental results.

Number	Factor			Measured values/MPa			Predicted values/MPa		
	X_1	X_2	X_3	Y_1	Y_2	Y_3	Y_1*	Y_2*	Y_3*
1	10	6	72	0.421	0.820	0.991	0.405	0.815	1.010
2	15	8	72	0.586	0.986	1.339	0.584	0.984	1.340
3	15	6	68	0.457	0.857	1.120	0.469	0.847	1.090
4	15	8	72	0.577	0.976	1.342	0.584	0.984	1.340
5	10	10	72	0.600	1.000	1.365	0.601	0.990	1.350
6	10	8	68	0.527	0.928	1.225	0.531	0.943	1.230
7	15	8	72	0.580	0.980	1.328	0.584	0.984	1.340
8	15	10	76	0.730	1.040	1.430	0.718	1.050	1.460
9	10	8	76	0.570	0.969	1.307	0.581	0.968	1.300
10	20	8	68	0.509	0.909	1.208	0.498	0.909	1.220
11	15	8	72	0.586	0.986	1.337	0.584	0.984	1.340
12	15	8	72	0.592	0.992	1.334	0.584	0.984	1.340
13	15	6	76	0.543	0.943	1.267	0.548	0.948	1.260
14	20	10	72	0.555	0.955	1.315	0.571	0.960	1.290
15	20	6	72	0.439	0.839	1.105	0.438	0.849	1.120
16	15	10	68	0.634	1.034	1.395	0.629	1.030	1.410
17	20	8	76	0.620	1.020	1.365	0.616	1.010	1.360

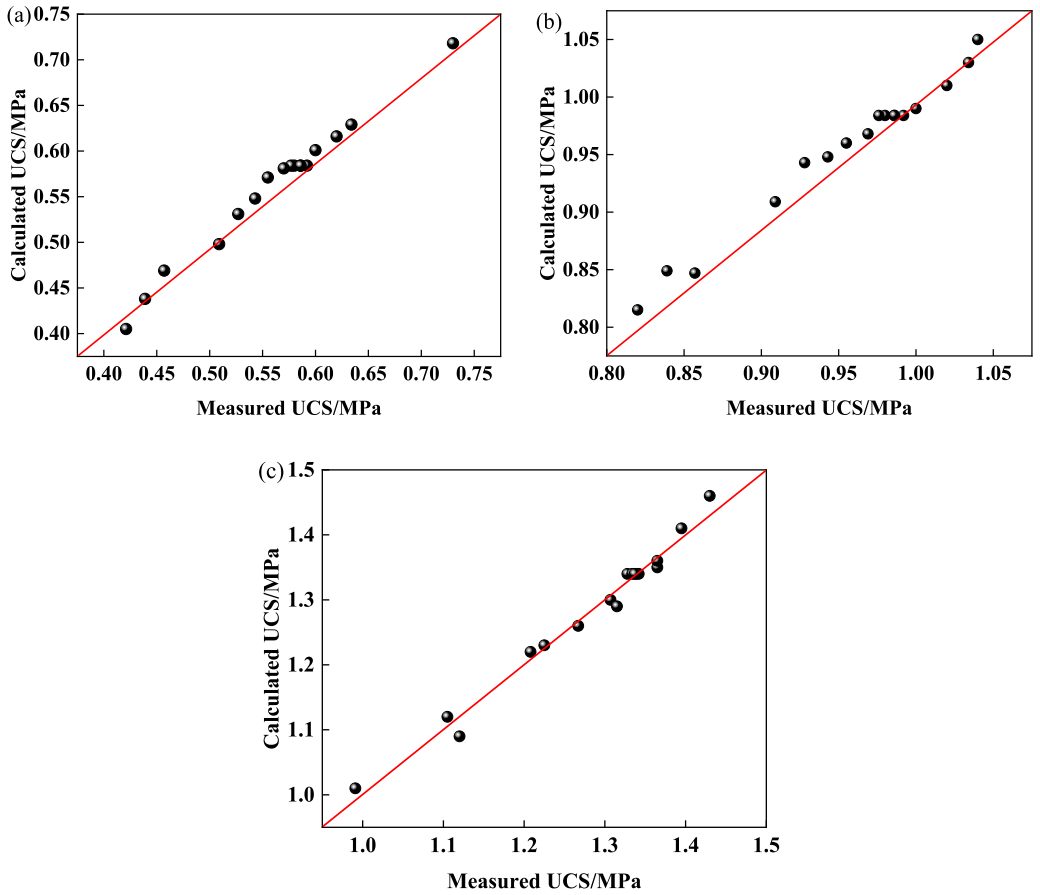

Fig. 2. Comparison between measured values and calculated values: (a) 7d UCS; (b) 14d UCS; (c) 28d UCS.

(highly significant), which indicates that the regression models are highly credible. The minimum value of the F-value of the 3 RSM models is 48.49(much higher than $F_{0.95}(3,9)= 3.86$), indicating that the regression results are highly significant and statistically significant. The correlation coefficients R^2 (e.g., Eqs. 3–5) are 0.9863, 0.9842, and 0.9853 converging to 1, indicating that the model fits well, and the error between experimental and predicted values is small, which is able to adequately respond to the relationship between the response values and the various effect factors. Among the factors, the single factor items: X_2 (binder dosage, $P < 0.01$) and

Table 7
Analysis of RSM model.

Variant source	Square sum			Average square			F-value			P-value		
	Y_1	Y_2	Y_3	Y_1	Y_2	Y_3	Y_1	Y_2	Y_3	Y_1	Y_2	Y_3
Item	0.0900	0.0674	0.2126	0.0100	0.0075	0.0236	56.03	48.49	51.98	< 0.0001	< 0.0001	< 0.0001
X_1	0.0000	0.0000	0.0014	0.0000	0.0000	0.0014	0.01	0.04	3.01	0.9116	0.8521	0.1261
X_2	0.0543	0.0406	0.1306	0.0543	0.0406	0.1306	304.09	262.87	287.32	< 0.0001	< 0.0001	< 0.0001
X_3	0.0141	0.0074	0.0221	0.0141	0.0074	0.0221	79.10	48.11	48.53	< 0.0001	0.0002	0.0002
$X_{1\times2}$	0.0010	0.0010	0.0067	0.0010	0.0010	0.0067	5.56	6.63	14.74	0.0505	0.0368	0.0064
$X_{1\times3}$	0.0012	0.0012	0.0014	0.0012	0.0012	0.0014	6.46	7.97	3.09	0.0385	0.0256	0.1220
$X_{2\times3}$	0.0000	0.0016	0.0031	0.0000	0.0016	0.0031	0.14	10.38	6.86	0.7220	0.0146	0.0345
X_{12}	0.0138	0.0090	0.0300	0.0138	0.0090	0.0300	77.50	58.37	65.97	< 0.0001	0.0001	< 0.0001
X_{22}	0.0022	0.0049	0.0139	0.0022	0.0049	0.0139	12.49	31.70	30.68	0.0095	0.0008	0.0009
X_{32}	0.0038	0.0015	0.0026	0.0038	0.0015	0.0026	21.07	9.51	5.62	0.0025	0.0177	0.0496

X_3 (slurry concentration, $P < 0.01$) had the most significant effect on Y(UCS). The interaction factor item: $X_1 \times_2$ (interaction between SF dosage and binder dosage, $P < 0.01$) has the most significant effect on Y_3 (28d UCS).

3.2. UCS analysis

3.2.1. The effect of a single factor on UCS

(1) Binder dosage

When the slurry concentration is 72 % and the SF dosage is 15 %, the relationship between binder dosage and UCS at curing time is shown in Fig. 3(a). From Fig. 3(a), the UCS of SCPB at different curing times increases with the increase in binder dosage. When the binder dosage increases from 6 % to 10 %, the 7d UCS, 14d UCS, and 28d UCS increase by 35 %, 16 %, and 22 %, respectively. Combined with the F-value of X_2 in the RSM model for the 7d in Table 7, it indicates that the binder dosage has a significant effect on early strength. Binder reacts with water during the early stages of hydration to form ettringite (AFt) and C-S-H, which provide early strength. These hydration products grow within the pores of the material, effectively filling the space previously occupied by free water and reducing the porosity of the aggregate, thereby providing a compact and robust structure for SCPB. An increase in the binder dosage leads to an increase in hydration products, thereby enhancing the UCS of SCPB.

(2) Slurry concentration

When the binder dosage is 8 % and the SF dosage is 15 %, the relationship between slurry concentration and UCS at different curing times is shown in Fig. 3(b). From Fig. 3(b), the UCS of SCPB at different curing times increases gradually as the slurry concentration increases. The higher the slurry concentration, the more significant the increase in UCS. When the slurry concentration increases from 68 % to 76 %, the 7d, 14d, and 28d UCS of SCPB increase by 15 %, 6 %, and 8 %, respectively. This indicates that slurry concentration has a significant effect on the early UCS of SCPB, consistent with the analysis results of the P-value in Table 7. Slurry concentration directly determines the water content in the reaction system. During the early stages of hydration, when hydration products are scarce, the slurry concentration directly affects the structural density of SCPB (higher concentration results in lower water content and a more dispersed structure), thereby affecting its early strength.

(3) SF dosage

When the binder dosage is 8 % and the slurry concentration is 72 %, the relationship between SF dosage and UCS at different curing

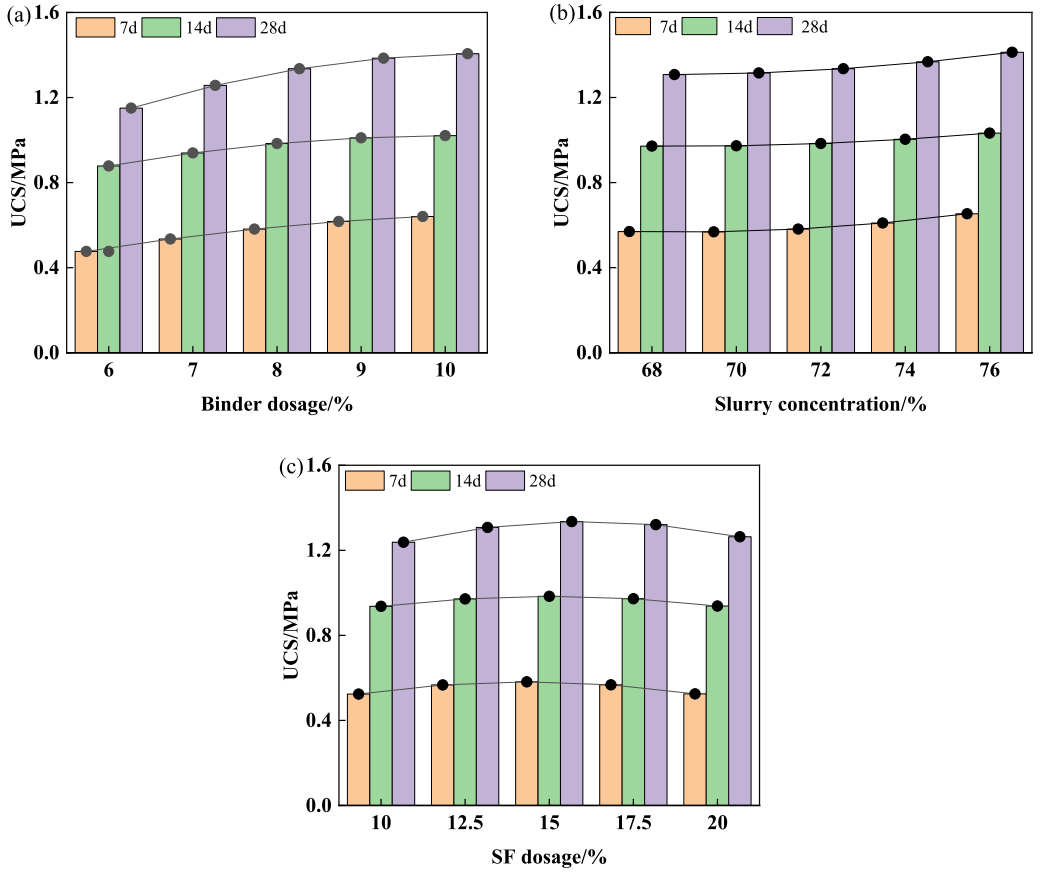

Fig. 3. UCS development patterns under single factor effects.

times is shown in Fig. 3(c). From Fig. 3(c), the UCS of SCPB at all curing time first increases and then decreases with increasing SF dosage. When the SF dosage is around 15 %, the UCS of SCPB at all curing times reaches its maximum, indicating that an appropriate SF dosage is beneficial for improving UCS. When the SF dosage increases from 10 % to 15 %, the UCS gradually increases. This is because an appropriate amount of fine-grained SF can fill the pores formed by coarse aggregates, which is conducive to improving the packing density of SCPB and thereby improving UCS. When the SF dosage is increased from 15 % to 20 %, UCS gradually decreases. This is because although fine aggregates can fill pores, excessive SF increases the porosity of SCPB, thereby reducing its packing density.

3.2.2. The effect of coupling factors on UCS

(1) SF dosage and slurry concentration

Fig. 4 presents the effect of SF dosage and slurry concentration on the 7d UCS of SCPB. Within the SF dosage range of 10 %–20 %, the 7d UCS consistently increases with increasing slurry concentration. When the slurry concentration is 68 %–76 %, the 7d UCS first increases and then decreases with increasing SF dosage. When the SF dosage is 10 % and the slurry concentration increases from 68 % to 76 %, the 7d UCS of SCPB increases by 9.45 %. When the SF dosage is 15 % and the slurry concentration increases from 68 % to 76 %, the 7-day UCS of SCPB increases by 14.56 %. This indicates that when the aggregate gradation is optimal, increasing the slurry concentration helps enhance early strength development. This is because, during the early stages of hydration, strength primarily originates from the support provided by the aggregates. Optimal gradation improves aggregate packing density, thereby enhancing early strength.

(2) Binder dosage and slurry concentration

Fig. 5 displays the effect of the coupled interaction between binder dosage and slurry concentration on the 14d UCS of SCPB. As can be observed, the 14d UCS increases with both the binder dosage and slurry concentration, indicating that the interaction between the dosage of the binder dosage and the slurry concentration exhibits a synergistic effect in enhancing strength. When the slurry concentration is 68 %, increasing the binder dosage from 6 % to 10 % results in a 21.58 % increase in 14d UCS. When the slurry concentration is 76 %, increasing the binder dosage from 6 % to 10 % results in a 10.82 % increase in 14d UCS. Thus, at lower slurry concentrations, the increase in 14d UCS due to higher binder dosage is more significant. This is because at lower slurry concentrations, the relative water content is higher, allowing the active components in the binder to react more thoroughly with water through hydration, thereby forming hydration products more rapidly and significantly enhancing the compressive strength of SCPB during the mid-curing stage.

(3) Binder dosage and SF dosage

Fig. 6 indicates the coupled effect of SF dosage and binder dosage on the 28d UCS of SCPB. The results show that when the SF dosage remains constant, the 28d UCS increases gradually with the increase in binder dosage. When the binder dosage exceeds 8 %, the rate of strength increase begins to slow down. This is because, in the later stages of the hydration reaction, the available water is insufficient to support the excess binder in producing additional active components, leading to a slower rate of strength development. When the binder dosage is 10 % UCS increases with increasing SF dosage, reaching a maximum at 14 % SF dosage, and then decreases with further increases in SF dosage. This indicates that an appropriate SF dosage can optimize the aggregate grading, promote the formation of a stable interlocking structure, and thereby form a more dense and uniform overall structure during the cementation process, significantly enhancing the late-stage strength of SCPB.

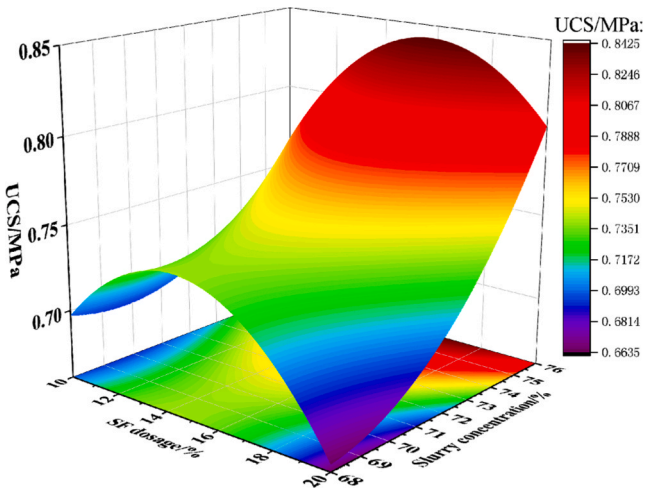

Fig. 4. The effect of SF dosage and slurry concentration on the 7d UCS of SCPB.

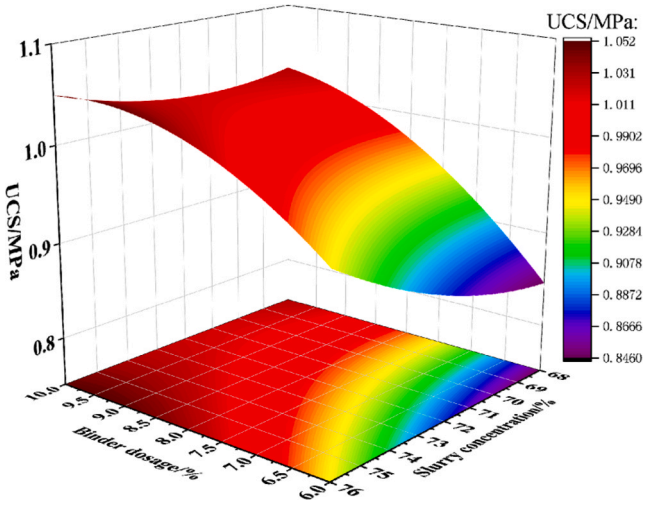

Fig. 5. The effect of binder dosage and slurry concentration on the 14d UCS of SCPB.

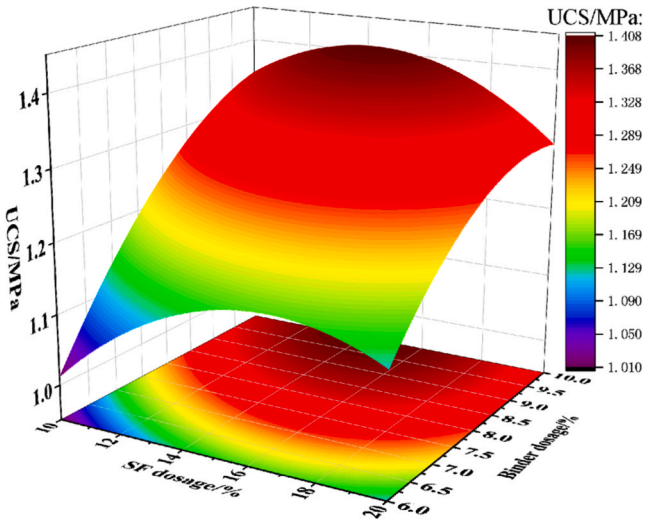

Fig. 6. The effect of binder dosage and SF dosage on the 28d UCS of SCPB.

3.3. Microanalysis

3.3.1. SEM

The microstructure of SCPB is obtained using SEM, and the images are binarized using Image J software [29,30] to construct two-dimensional and three-dimensional grayscale images of SCPB with a curing time of 28 d, as shown in Fig. 7. The internal microstructure of SCPB mainly consists of pores, aggregate particles, and hydration products. Hydration products grow within the porous structure formed by aggregate particles, continuously consuming and occupying the space occupied by free water, effectively filling and bonding aggregate particles to form a high-strength microstructure. 4 groups of samples (1, 3, 11, and 16) from Table 5 are selected for SEM microstructural analysis. In sample 1, a certain amount of short columnar AFt crystals (average length approximately 2 μm) and loosely distributed C-S-H gel and flaky $Ca(OH)_2$ (CH) are observed, with large pores between aggregate particles. In sample 3, the number of hydration products increased significantly, with the average length of AFt crystals growing to 2–4 μm. These crystals are densely distributed with C-S-H in the pores, leading to a gradual reduction in pore number and size. In sample 11, the continuously accumulating gel-like C-S-H binds AFt and aggregate particles together, giving the SCPB structure a dense characteristic. In sample 16, under the synergistic action of C-S-H gel, AFt crystals, and other hydration products, the pores within the SCPB are fully filled.

Compared with sample 3, the microstructural images of sample 16 show almost no pores, with a smoother and more uniform three-dimensional gray-scale structure, indicating a more dense structure. Under constant SF dosage and slurry concentration, the three-dimensional grayscale images of sample 16 show a significant reduction in low-lying areas, indicating lower porosity and a more dense structural characteristic. Compared with sample 1, although the aggregate packing density of sample 11 decreased, the 28d UCS

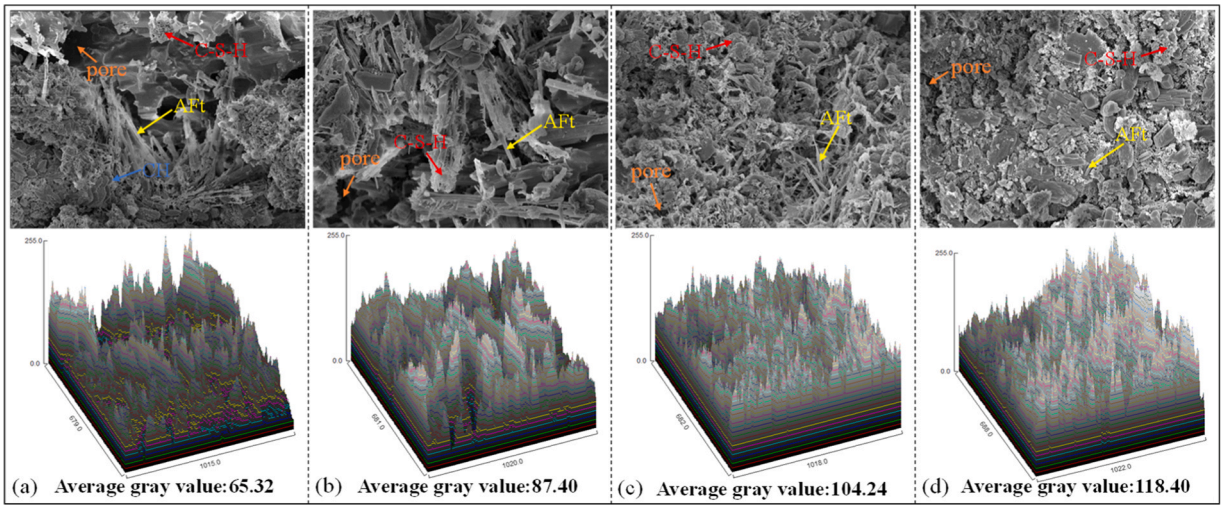

Fig. 7. Microstructure: (a) Sample 1; (b) Sample 3; (c) Sample 11; (d) Sample 16.

increased from 0.991 MPa to 1.337 MPa, and the average grayscale value improved from 65.32 to 104.24 by increasing the binder dosage. This indicates that a denser microstructure (due to more hydration products filling the pores) results in higher strength. This is because the increased binder dosage directly enhanced the production of hydration products, effectively filling the pores, resulting in higher density and improved mechanical properties.

3.3.2. XRD

The mineral phases of SCPB are shown in Fig. 8. Characteristic peaks of hydrated products such as hydrocalumite and AFt are observed in samples with curing times of 7 d and 28 d. Characteristic peaks of dehydrated gypsum($CaSO_4{\cdot}2H_2O$), quartz, calcite, dolomite, C_2S, RO phase, and C_3S are also observed in the raw materials [31,32]. The intensity of the characteristic peaks of dehydrated gypsum, C_2S, and C_3S decreases gradually with increasing curing age, indicating that these hydrolyzable substances are continuously consumed. Compared to the 7d-cured samples, the intensity of the hydrocalumite diffraction peak ($2\theta = 12.5°$) and the AFt diffraction peaks ($2\theta = 25°, 28°$) in the 28d-cured samples significantly increased. Additionally, a more pronounced AFt diffraction peak appeared near $2\theta = 8.5°$, indicating an increasing amount of hydration products, which is a key factor contributing to the improvement of 28d UCS.

Compared to sample 3, sample 16 exhibited significantly enhanced diffraction peaks of hydrocalumite near $2\theta = 12.5°$ and AFt diffraction peaks near $2\theta = 25°$ and $28°$ after increasing the binder dosage. Therefore, the strength of sample 16 is significantly improved. The XRD patterns of sample 11 show a significant increase in hydration products compared to sample 1 (as evidenced by the enhanced intensity of the AFt diffraction peaks near $2\theta = 8.5°$, $25°$, and $28°$, and the hydrocalumite diffraction peak near $2\theta = 12.5°$), resulting in higher strength. This is because increasing the binder dosage directly increases the amount of active components in the hydration reaction, significantly enhancing the quantity of hydration products and strength in the sample.

It is worth noting that the AFt diffraction peak ($2\theta \approx 8.5°$) in the XRD pattern becomes much more pronounced at 28d than at 7d

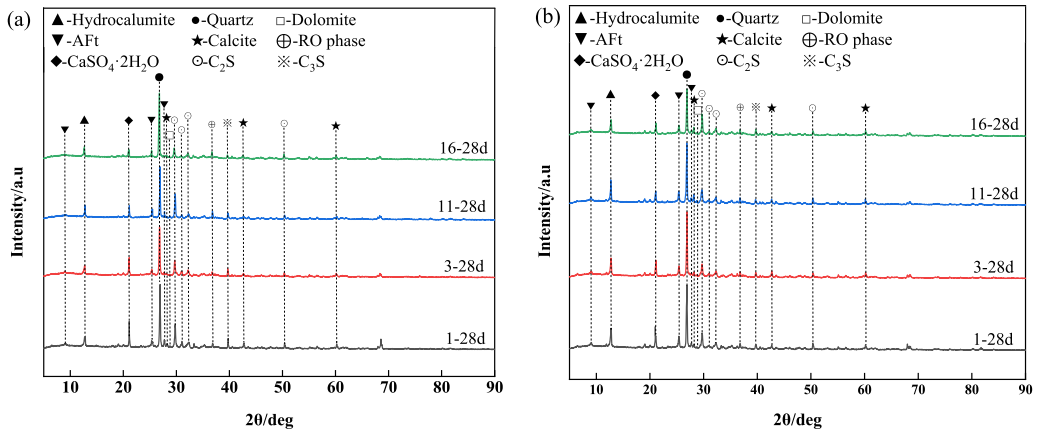

Fig. 8. XRD patterns of SCPB at different curing times: (a) 7d; (b) 28d.

(nearly doubling in intensity), which quantitatively reflects an increase in AFt content.

3.3.3. FTIR

The FTIR results for SCPB with curing times of 7d and 28d are shown in Fig. 9. The absorption peaks at 3400 cm^{-1} and 1630 cm^{-1} correspond to the asymmetric stretching vibration and bending vibration of the O-H bond in the crystalline water of the hydration product, respectively [33]. Compared with the sample with a curing time of 7d, the transmittance of the above 2 absorption peaks is significantly weakened at a curing time of 28d, indicating the formation of a large amount of crystalline water-rich material. The absorption peak at 3630 cm^{-1} corresponds to the stretching vibration of the O-H bond in dihydrate gypsum. The absorption peaks at 1435 cm^{-1} and 875 cm^{-1} correspond to the stretching vibration and bending vibration of the C-O bond, respectively [34]. This is caused by the carbonization reaction of SCPB during the curing process. The absorption peaks at 1010 cm^{-1} and 470 cm^{-1} correspond to the asymmetric stretching vibrations of the Si-O-Si bonds in C-S-H [35]. Si in GBFS is a typical network-forming element, primarily forming Si-O bonds with oxygen, which then polymerize into SiO_4^{4-} tetrahedra, SiO_7^{6-} clusters, chains, and other polymerized products of silicate anions, ultimately forming a three-dimensional network structure of glass. This network structure facilitates the formation of a stable C-S-H gel network, significantly enhancing the density and stability of the filling material.

Compared to sample 3, sample 16 shows a decrease in the transmittance of absorption peaks at 3400 cm^{-1}, 1630 cm^{-1}, 1010 cm^{-1}, and 470 cm^{-1}, which represent hydration products, while the absorption peak at 3630 cm^{-1}, which represents the reactant, significantly increases. This indicates that dihydrate gypsum is gradually consumed, and hydration products gradually increase. This is consistent with the XRD analysis results. Comparing the FTIR spectra of samples 1 and 11, despite a decrease in the packing density of the mixed aggregate after reducing the SF dosage from 15 % to 10 %, increasing the binder dosage from 6 % to 8 % directly provided more reactants for the hydration reaction, leading to an increase in hydration products (the transmittance of the characteristic peaks at 3400 cm^{-1}, 1630 cm^{-1}, 1010 cm^{-1}, and 470 cm^{-1} in sample 11 was significantly lower than that in sample 1), thereby enhancing the strength.

3.3.4. The formation mechanism of SCPB strength

This study utilized a ternary composite binder prepared from SS, GBFS, and FDG. SS serves as an important alkaline activator, providing the necessary alkaline environment for hydration reactions and promoting the depolymerization and hydration of the silica-alumina glassy structure in GBFS. FDG, as a sulfate activator, supplies a large amount of SO_4^{2-} during hydration reactions, reacting with Ca^{2+} and Al^{3+} in SS and GBFS to form AFt [36,37]. GBFS serves as the active component in the ternary composite cementitious system, with its abundant amorphous glass phase conferring high potential activity [38–40]. Under the combined action of alkaline activators and sulfate activators, the glass phase in the slag undergoes depolymerization, thereby providing active Si/Al groups for the hydration reaction.

During the initial stage of the hydration reaction, various substances begin to dissolve and release ions. FDG provides Ca^{2+} and SO_4^{2-} (Eq. 6). C_2S and C_3S in SS both dissolve CH and generate a small amount of C-S-H (Eqs. 7 and 8). As Ca^{2+} dissolves, the silicon-oxygen tetrahedra and aluminum-oxygen tetrahedra in GBFS undergo depolymerization and repolymerization, dissolving in the form of $[SiO_4]$ and $[AlO_4]$, respectively (Eqs. 9 and 10). Additionally, under the action of OH^-, octahedral $AI(OH)_6^{3-}$ ions are dissolved, which are the key units for forming AFt and can react with Ca^{2+}, OH^-, and SO_4^{2-} to form AFt (Eq. 11). During the mid-stage of the hydration reaction, hydration products gradually form. As large amounts of Ca^{2+} dissolve and AFt is generated, $[SiO_4]$ and $[AlO_4]$ in GBFS continuously polymerize with Ca^{2+} and water molecules to form C-S-H (Eqs. 12 and 13). In addition, when SO_4^{2-} is sufficient in the system, $[AlO_4]$ reacts with SO_4^{2-} to form AFt (Eq. 14). In the late stage of the hydration reaction, AFt crystals develop fully in the system, forming a more slender needle-like structure that can fill the pores, effectively reducing the porosity of SCPB. Concurrently, the abundant formation of C-S-H, with its dense network structure, further binds the aggregates and hydration products in the SCPB. This bonding structure formed by the synergistic action of AFt and C-S-H significantly enhances the density and mechanical properties of the SCPB.

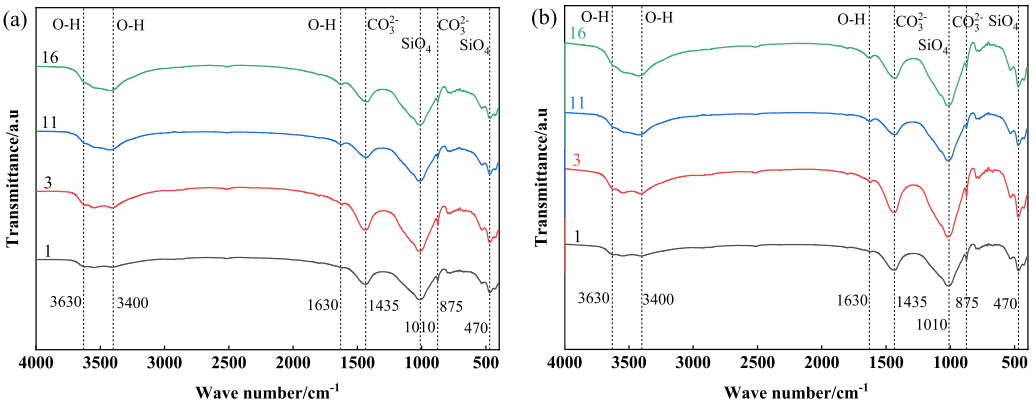

Fig. 9. FTIR spectra of SCPB with different curing times: (a) 7d; (b) 28d.

$$CaSO_4 \cdot 2H_2O \rightarrow Ca^{2+} + SO_4^{2-} + 2H_2O \quad (6)$$

$$C_2S + H_2O \rightarrow C-S-H + Ca(OH)_2 \quad (7)$$

$$C_3S + H_2O \rightarrow C-S-H + Ca(OH)_2 \quad (8)$$

$$AlO_4^{5-} + H_2O \rightarrow H_3AlO_4^{2-} + 3OH^- \quad (9)$$

$$SiO_4^{4-} + H_2O \rightarrow H_3SiO_4^- + H_2SiO_4^{2-} + OH- \quad (10)$$

$$\{Ca_6[Al(OH)_6]_2 24H_2O\}^{6+} + SO_4^{2-} + H_2O \rightarrow \{Ca_6[Al(OH)_6]_2 24H_2O\}[3SO_4 2H_2O] \quad (11)$$

$$H_3SiO_4^- + H_2SiO_4^{2-} + Ca^{2+} + H_2O \rightarrow nCaO \cdot mSiO_2 \cdot zH_2O \quad (12)$$

$$H_3SiO_4^- + H_2SiO_4^{2-} + Ca^{2+} + H_3AlO_4^{2-} + H_2O \rightarrow nCaO \cdot mSiO_2 \cdot yAl_2O_3 \cdot zH_2O \quad (13)$$

$$H_2SiO_4^{2-} + 3Ca^{2+} + OH^- + CaSO_4 \cdot 2H_2O + 44H_2O \rightarrow 3CaO \cdot Al_2O_3 \cdot 3CaSO_4 \cdot 32H_2O \quad (14)$$

4. Machine learning-based proportion design for SCPB

In this research, MAA is used to optimize particle size distribution to improve packing density, RSM is employed to design and analyze the experiments efficiently, Extreme Learning Machine (ELM) is chosen for its fast learning capability to model UCS, Sparrow Search Algorithm (SSA) is applied to fine-tune the ELM hyperparameters, and Genetic Algorithm (GA) is utilized to invert the model for optimal mix proportions.

4.1. Construction process of the machine learning prediction model

The SSA and GA are both random global search optimization methods developed based on biological systems, capable of finding optimal solutions to complex nonlinear problems [41,42]. ELM is a single-layer feedforward neural network based on randomization, featuring fast learning speed, high accuracy, and ease of implementation, making it a powerful tool for multi-variable nonlinear modeling [41,42]. This study uses SSA to optimize the hyperparameters of ELM, constructs an SSA-ELM model for predicting the strength of SCPB, and then employs GA to perform inverse optimization on the SSA-ELM model under a given target strength to identify the optimal mixture proportion. Additionally, support vector regression(SVR), XGBoost, and random forest(RF) [43–46], which are similar to ELM, are used as controls. The specific modeling steps are as follows.

Using the results of 51 RSM experiments as the data set, the SF dosage, binder dosage, and slurry concentration in the data set are used as input variables, and the UCS at different curing times are used as output variables. The dataset is preprocessed using normalization to eliminate the influence of different units on the model. The dataset is randomly divided into an 80 % training set and a 20 % validation set to train and evaluate the predictive performance of the model. Due to the small size of the dataset, to avoid

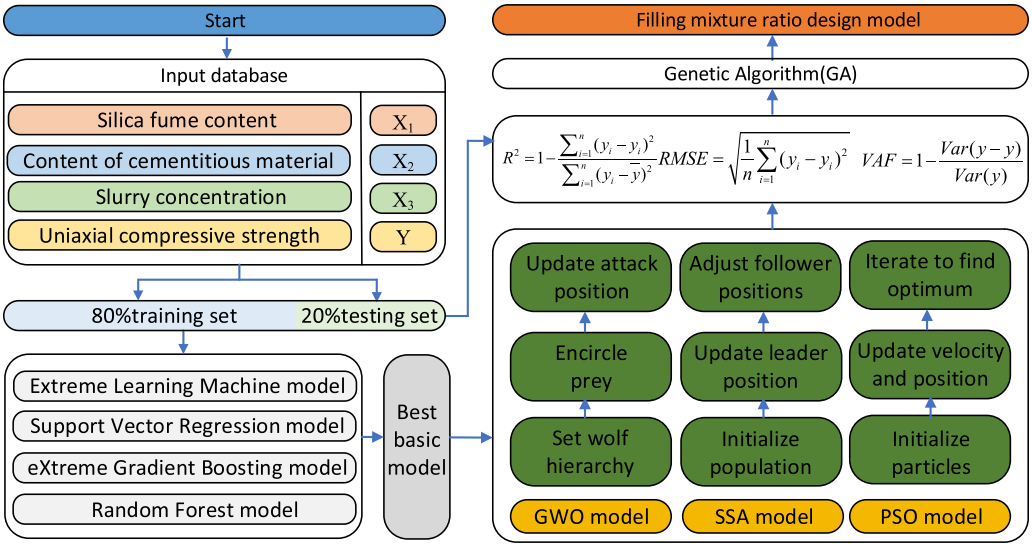

Fig. 10. Process of constructing a machine learning prediction model.

overfitting, all models were trained using 5-fold cross-validation. Finally, SSA, ELM, and GA are combined to achieve collaborative modeling, constructing a machine learning prediction model aimed at finding the optimal mixing ratio of coupled factors for multiple objectives. The model construction process is shown in Fig. 10.

4.2. Construction and optimization of the model

4.2.1. Construction of a basic model

To select the basic model with the best predictive performance as the basic model for the SCPB proportion design optimization, 3 evaluation indicators, R^2, RMSE, and VAF, are used to characterize the predictive performance of ELM, SVR, XGBoost, and RF. To ensure fairness in the comparison of the basic models, the parameters are adjusted in advance so that each model achieves its optimal predictive performance. The predictive performance of the different basic models is as follows.

(1) ELM

In the ELM model, the number of hidden layer neurons has the most significant effect on the prediction performance of ELM. Too many neurons can lead to overfitting of the model, while too few neurons can lead to underfitting. Therefore, to obtain the optimal performance of ELM, the 10-fold cross-validation method is used to evaluate the performance of the model under different numbers of hidden layer neurons, and the optimal number of hidden layer neurons is obtained. Fig. 11 shows that when the number of hidden layer neurons is 42, the fitness value is minimal. Therefore, the optimal number of hidden layer neurons for the ELM is 42. Substituting the optimal hyperparameters into the ELM yields the prediction result marginal histogram shown in Fig. 12(a). This shows that the measured values and predicted values of the ELM are uniformly and compactly distributed on both sides of the y = x line. The training set has $R^2 = 0.9275$, RMSE = 0.0851, and VAF = 92.7813, while the testing set has $R^2 = 0.9123$, RMSE = 0.0792, and VAF = 91.3977, indicating that the ELM has excellent prediction performance.

(2) SVR

In the SVR model, the regularization parameter (C) and the implicit parameter (γ) have the most significant effect on the prediction performance of the SVR model. The grid search method (GSM) finds the optimal parameters by specifying multiple candidate values for C and γ and traversing all possible combinations of these values. The search range for C is set to (0.1, 100), and the search range for γ is set to (0.001, 1). After the search, best_C = 1.4915 and best_γ = 0.5924. Substituting the optimal hyperparameters into the SVR model yields the prediction results marginal histogram shown in Fig. 12(b). This shows that the measured values and predicted values of the SVR model are uniformly distributed on both sides of the line of y = x. The training set has an R^2 of 0.8582, RMSE of 0.1177, and VAF of 85.9046, while the testing set has an R^2 of 0.8025, RMSE of 0.1188, and VAF of 80.6624, indicating that the SVR model has good predictive performance.

(3) XGBoost model

In the XGBoost model, the maximum decision tree depth (max_depth), learning rate (learning_rate), and L2 regularization coefficient (reg_lambda) have the most significant effects on the prediction performance of the XGBoost model. Similarly, the XGBoost model is tuned to its optimal state using the GSM. After searching, when max_depth = 6, learning_rate = 0.042, and reg_lambda = 0.08, the prediction performance of the XGBoost model reached its optimal state. The prediction result marginal histogram is shown in Fig. 12(c). The measured values and predicted values of the XGBoost model are scattered on both sides of the straight line of y = x. The training set has an R^2 of 0.7548, RMSE of 0.1566, and VAF of 75.9027, while the testing set has an R^2 of 0.6484, RMSE of 0.1585, and VAF of 65.5663, indicating that the predictive performance of the XGBoost model is average.

(4) RF model

In the RF model, the number of decision trees (n_estimators) and the maximum depth of decision trees (max_depth) have the most significant effect on the prediction performance of the RF model. Therefore, random search is first used for preliminary parameter screening, and then Bayesian optimization is used in a smaller range to fine-tune the parameters until the RF model achieves the best prediction performance. The optimal parameters obtained by random search are n_estimators= 500 and max_depth= 5, and the optimal parameters after fine-tuning with Bayesian optimization are n_estimators= 476 and max_depth= 23. The marginal histogram of the prediction results obtained when the RF model reaches its optimal state is shown in Fig. 12(d). It shows that the measured values and predicted values of the RF model are significantly offset on both sides of the line(y = x). The training set has an R^2 of 0.7076, RMSE of 0.1710, and VAF of 72.3840, while the testing set has an R^2 of 0.7032, RMSE of 0.1456, and VAF of 70.7952. This indicates that the RF model has poor predictive performance.

4.2.2. Construction of a basic model

In the comparison of the predictive performance of the above-mentioned basic models, ELM outperformed other models in all evaluation metrics. This indicates that ELM has stronger robustness and can accurately predict the nonlinear relationship between multi-objective coupling factors and UCS. Therefore, ELM is selected as the basic model for the optimization of the combination proportion in SCPB.

In this study, 3 optimization algorithms—SSA, particle swarm optimization (PSO), and gray wolf optimization (GWO) [47,48]—are employed to further optimize the hyperparameters of the ELM model, thereby enhancing its predictive performance. To ensure that all algorithms achieve optimal optimization results under the same conditions, the maximum number of iterations for all algorithms is set to 100, and the population size is set to 40. A 10-fold cross-validation method is used to determine the optimal number of hidden layer nodes and the initial learning rate for the ELM model. The results of optimizing different base models are as follows.

(1) SSA-ELM

SSA is used to optimize ELM, and the optimization results of SSA-ELM are as follows: optimal number of hidden layer nodes = 15,

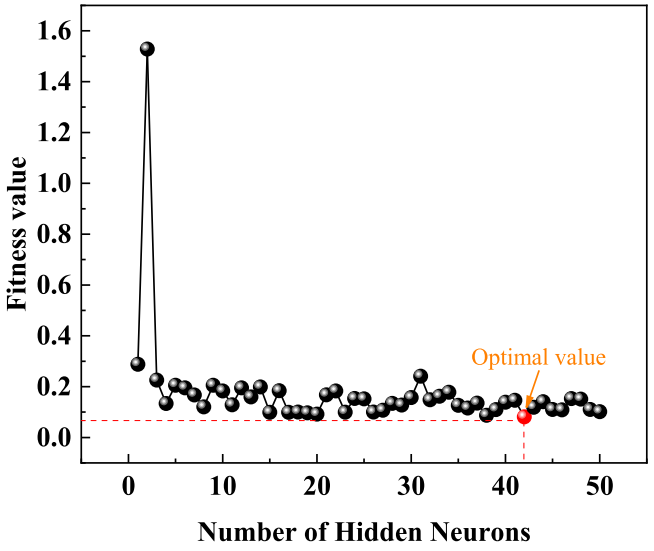

Fig. 11. Relationship between the number of hidden layer neurons and fitness.

optimal initial learning rate = 0.0287. The dataset is substituted into the optimal SSA-ELM for training, and the UCS prediction results and error distributions of the training set and test set of SSA-ELM are shown in Fig. 13. As Fig. 13(a) indicates, the prediction performance of SSA-ELM is good (R^2 = 0.9811, RMSE = 0.0542, VAF = 94.8303). The ELM optimized by the SSA algorithm demonstrates a significant improvement in prediction performance, with measured values and predicted values showing high consistency. From Fig. 13(b), it can be seen that the 95 % prediction interval and 95 % confidence interval of SSA-ELM are both narrow, and the predicted data points are all located within the 95 % prediction band, concentrated around the 95 % confidence interval and the ideal curve. In summary, SSA demonstrates outstanding effectiveness in optimizing ELM, significantly improving the predictive accuracy and generalization ability of the model, and validating its strong advantages in enhancing ELM performance.

PSO is used to optimize ELM, and the optimization results of PSO-ELM are: optimal number of hidden layer nodes = 22, optimal initial learning rate = 0.0398. The UCS prediction results and error distribution of the training set and testing set of PSO-ELM are shown in Fig. 14. As can be seen from Fig. 14(a), PSO-ELM achieves good prediction performance (R^2 = 0.9051, RMSE = 0.0942, VAF = 82.6303), but it is inferior to SSA-ELM. The distribution of measured values and predicted values exhibits a dispersed characteristic. From Fig. 14(b), the predicted data of PSO-ELM are mostly within the 95 % prediction interval, but they are relatively dispersed near the 95 % confidence interval and the ideal curve. In summary, PSO effectively optimizes ELM.

(3) GWO-ELM

GWO is used to optimize ELM, and the optimization results of GWO-ELM are as follows: the optimal number of hidden layer nodes = 12, and the optimal initial learning rate = 0.0377. The UCS prediction results and error distribution of the training set and testing set of GWO-ELM are shown in Fig. 15. From Fig. 15(a), it can be seen that the prediction performance of GWO-ELM is generally average (R^2 = 0.8956, RMSE = 0.1142, VAF = 83.6679), with significant dispersion between the measured and predicted data points. Fig. 15 (b) shows that the 95 % prediction interval and 95 % confidence interval of GWO-ELM are both relatively wide, and the predicted data points are highly dispersed. This indicates that the optimization effect of GWO on ELM is poor.

4.2.3. Determination of the optimal model

During the optimization of the basic model, ELM exhibits varying degrees of improvement in predictive performance after optimization by SSA, PSO, and GWO. Based on the evaluation indices of each model, SSA-ELM performs the best, with all evaluation indices (R^2 = 0.9811, RMSE = 0.0542, VAF = 94.8303) significantly better than ELM, PSO-ELM, and GWO-ELM. To further quantify the performance of different models, the optimization model ranking method is introduced [49], with the ranking results shown in Table 8. Based on the comprehensive evaluation results, SSA-ELM is the optimal prediction model with the best predictive performance, and therefore it is selected as the optimal model in this study.

4.3. Filling mix proportion design and verification

To achieve high-precision prediction of SCPB strength and intelligent proportioning design, this study selects the optimal SSA-ELM as the basic model and combines it with GA to design an intelligent proportional design model for accurately predicting SCPB strength, namely the SSA-ELM-GA. The steps in the synergistic solution process of the SSA-ELM and GA model are as follows.

The first step is to define the objective function. A nonlinear function $f_{SSA\text{-}ELM}$ is constructed using SSA-ELM, and the nonlinear function $f_{SSA\text{-}ELM}$ is combined with the target UCS to form the objective function.

The second step is GA solution. The defined objective function is used as the fitness function in GA, and the GA is used for global

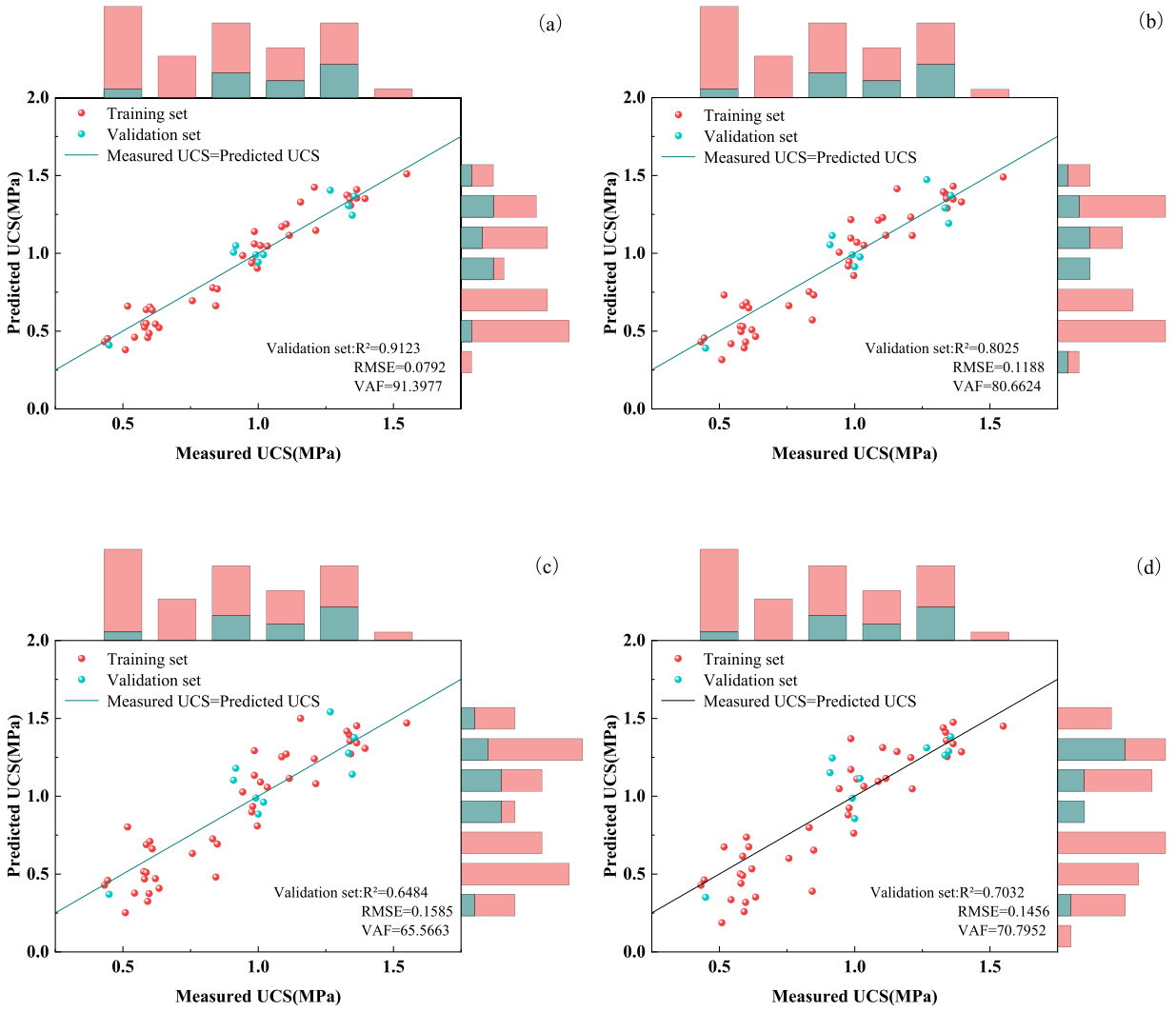

Fig. 12. Prediction results of the basic models: (a) ELM; (b) SVR; (c) XGBoost; (d) RF.

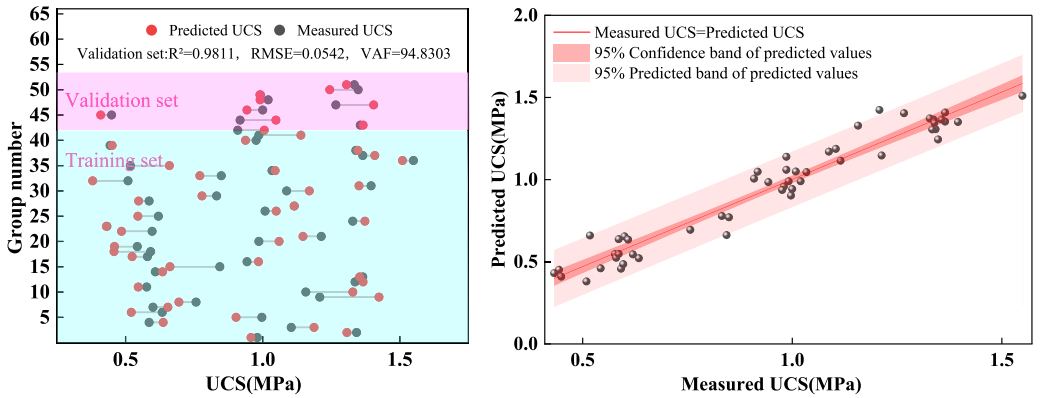

Fig. 13. SSA-ELM model: (a) Data comparison; (b) Confidence interval.

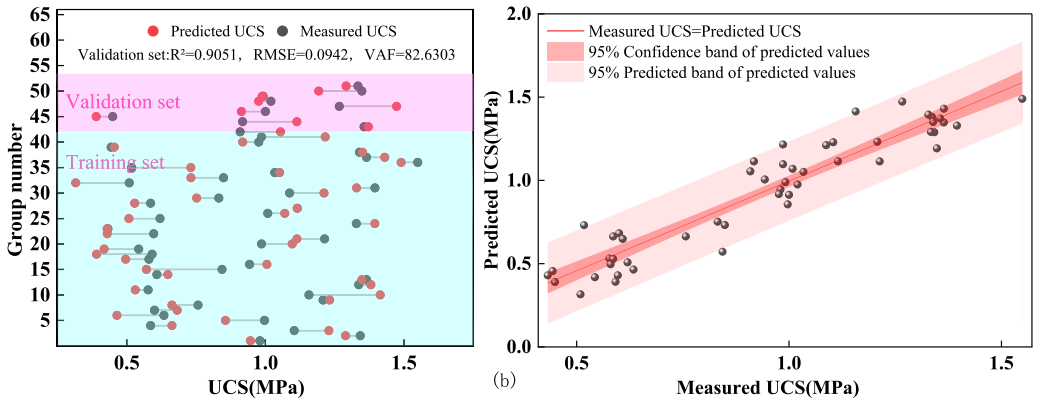

Fig. 14. PSO-ELM model: (a) Data comparison; (b) Confidence interval.

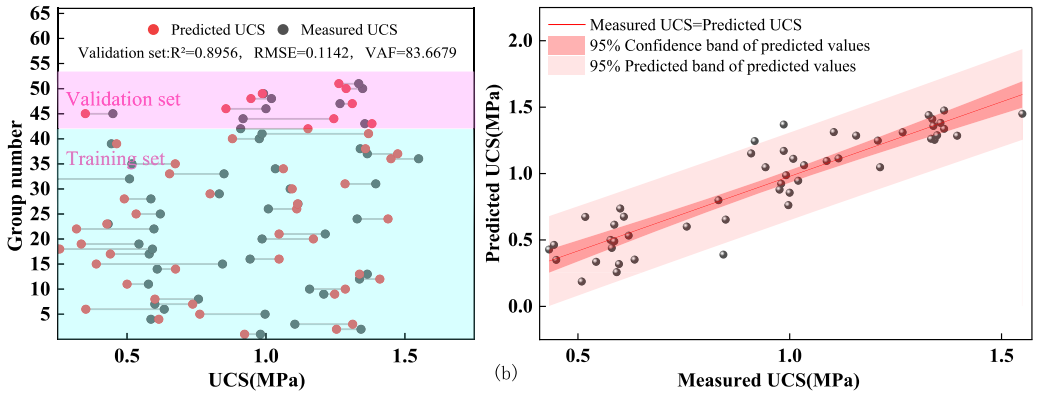

Fig. 15. GWO-ELM model: (a) Data comparison; (b) Confidence interval.

Table 8
Ranking of prediction performance of different models.

Method	Evaluation indices			Ranking of evaluation indices			Sum of sorts	Ranking
	R^2	RMSE	VAF	R^2	RMSE	VAF		
SSA-SVR	0.9811	0.0542	94.8303	3	3	3	9	3
PSO-SVR	0.9051	0.0942	82.6303	2	2	2	6	2
GWO-SVR	0.8956	0.1142	83.6679	1	1	1	3	1

search to find the minimum value of the fitness function, which is the optimal solution. The proportion corresponding to this optimal solution is the optimal proportion. This achieves accurate prediction of SCPB strength and intelligent design of proportions.

This study takes a large gold mine in Northeast China as the research case, with target values of 2 MPa and 3 MPa for the 28d UCS. Based on the above strength target values combined with the nonlinear function $f_{SSA\text{-}ELM}$, the objective function is formed as follows.

$$F_2 = \min\ (f_{SSA\text{-}ELM}\text{-}2)\ \text{s.t.}\ f_{SSA\text{-}ELM} \geq 2 \tag{14}$$

$$F_3 = \min\ (f_{SSA\text{-}ELM}\text{-}3)\ \text{s.t.}\ f_{SSA\text{-}ELM} \geq 3 \tag{15}$$

Table 9
Results and validation of the optimal SCPB proportion.

Objective function	Optimal proportion			28d UCS experimental verification value		
	X_1	X_2	X_3	Target UCS (MPa)	Measured value (MPa)	Relative error (%)
F_2	16.248	8.515	68.592	2.00	2.11	5.50 %
F_3	16.075	8.832	68.775	3.00	3.08	2.67 %

Based on existing research findings, this study adopted real number encoding for individual coding in the GA solution process, with a population size of 100, 100 evolutionary generations, a crossover probability of 0.4, and a mutation probability of 0.2. The optimal SCPB proportion is obtained using GA, as shown in Table 9. To verify the accuracy of the SSA-ELM and GA collaborative solution, further laboratory SCPB proportion experiments are conducted, with the experimental results also listed in Table 9. As shown in Table 9, the optimal SCPB proportions designed by SSA-ELM-GA yielded 7d UCS and 28d UCS of 2.11 MPa and 3.08 MPa, respectively, with relative errors of only 5.50 % and 2.67 % compared to the target values. This indicates that SSA-ELM-GA can accurately predict the strength of SCPB and quickly and accurately obtain the optimal backfill proportion that satisfies the constraints of actual engineering projects, thereby reducing cumbersome manual experiments and promoting the development of mining engineering toward high efficiency, low cost, and intelligence.

5. Conclusion

This study prepared SCBP using ST, SF, and FA as mixed aggregates and SS, FDG, and GBFS as binder. Based on the MAA model, the aggregate mix ratio is optimized to achieve the maximum aggregate packing density, resulting in the optimal mixed aggregate mix ratio of m(SF): m(FA): m(ST) as 10:20:70. The strength of SCPB at each curing time increases with the increase of binder dosage and slurry concentration. With the increase of SF dosage, the strength first increases and then decreases. The results of single factor analysis show that binder dosage and slurry concentration have a significant effect on strength, while SF dosage has no significant effect. Microstructural analysis revealed that the strength development mechanism of SCPB is closely related to the content of SF, FA, and ST. SF and FA release active components through hydration reactions, filling the pores of aggregates and improving packing density. ST provides the basic framework for SCPB. The ternary composite binbder used in this study consists of SS, GBFS, and FDG. SS activates the hydration reaction of GBFS, while FDG promotes the formation of AFt. During hydration, the generated AFt and C-S-H synergistically enhance the density and mechanical properties of SCPB. Based on the SSA-ELM-GA intelligent backfilling proportion design model, high-precision prediction of SCPB strength is achieved, enabling rapid and accurate determination of the optimal SCPB proportion, thereby reducing cumbersome manual experiments.

Future studies could further investigate the effects of different industrial solid waste combinations on the performance of SCPB, particularly focusing on the activation and synergistic effects of novel solid waste materials. Additionally, integrating more machine learning algorithms (e.g., deep learning) could optimize the mix proportion model, enhancing prediction accuracy and generalization. Research should also address long-term durability (e.g., impermeability, frost resistance) and environmental behavior (e.g., heavy metal leaching) to advance practical applications of green backfill technology. For micro-mechanisms, in-situ characterization techniques (e.g., X-CT) could reveal the dynamic formation process of hydration products, providing a more precise theoretical basis for material design. Finally, developing low-cost, high-efficiency industrial production processes is essential to promote large-scale implementation in mining engineering.

CRediT authorship contribution statement

Zhiyi Liu: Software, Resources, Project administration. **Sitao Zhu:** Writing – review & editing, Validation, Software, Methodology. **Lujing Zheng:** Validation, Software, Resources. **Bin Han:** Writing – review & editing, Validation, Investigation. **Yafei Hu:** Writing – review & editing, Writing – original draft, Validation, Software, Methodology, Investigation. **Ruipeng Hu:** Resources, Methodology, Investigation.

Declaration of Competing Interest

The authors declare that they have no known competing financial interests or personal relationships that could have appeared to influence the work reported in this paper.

Acknowledgements

This work is supported by the Postdoctoral Fellowship Program of CPSF (Grant Number: GZB20240060, China); China Postdoctoral Science Foundation (Grant Number: 2024M750187, China); National Natural Science Foundation of China（52374115，52204134）

Data Availability

Data will be made available on request.

References

[1] Z. He, F. Ju, M. Xiao, Effects of aggregate size and carbon fiber content on piezoresistive responses of smart coal waste-based cemented paste backfill, Constr. Build. Mater. 470 (2025) 140562, https://doi.org/10.1016/j.conbuildmat.2025.140562.
[2] J. Zheng, P. Bi, S. Li, Z. Yang, Effects of NaOH and gypsum contents on the properties of cemented paste backfill using NaOH/gypsum-activated slag binders, Constr. Build. Mater. 470 (2025) 140552, https://doi.org/10.1016/j.conbuildmat.2025.140552.
[3] C. Zhang, J. Wang, W. Song, J. Fu, The bonding mechanism of rock and cement paste backfill interface under high temperature curing, Powder Technol. 453 (2025) 120680, https://doi.org/10.1016/j.powtec.2025.120680.

[4] Z. Guo, J. Qiu, H. Jiang, Q. Zhu, J. Wang Kwek, L. Ke, Z. Qu, Experimental and modeling study on the transient flow and time-dependent yield stress of superfine-tailings cemented paste backfill, Constr. Build. Mater. 367 (2023) 130363, https://doi.org/10.1016/j.conbuildmat.2023.130363.
[5] K. Zhao, Y. Zhou, Q. Huang, S. Yin, Y. Yan, J. Wu, L. Shen, X. Zeng, W. Liu, Early properties and modeling of cemented superfine tailings backfill containing sodium dodecyl sulfate: microstructure, mechanics, and acoustics, Mech. Mater. 179 (2023) 104567, https://doi.org/10.1016/j.mechmat.2023.104567.
[6] B. Zhang, K. Li, D. Chen, B. Han, Y. Hu, B. Liu, Exploration of the use of superfine tailings and ternary solid waste-based binder to prepare environmentally friendly backfilling materials: hydration mechanisms and machine learning modeling, J. Environ. Chem. Eng. 13 (2) (2025) 115662, https://doi.org/10.1016/j.jece.2025.115662.
[7] C. Yang, H. Lin, R. Gao, Z. Li, D. Gan, M. Liu, Q. Ren, Mechanical behaviour analysis of cemented tailings rock backfill materials: an insight from mesoscale modelling coupled with damage plasticity model, Case Stud. Constr. Mater. 22 (2025) e04356, https://doi.org/10.1016/j.cscm.2025.e04356.
[8] Y. Hou, S. Yin, Y. Wang, X. Yu, X. Li, L. Wang, K. Yang, X. Huang, Mechanical properties and damage evolution mechanisms of cemented backfill with tailored particle size range of coal gangue aggregates, Process Saf. Environ. 198 (2025) 107123, https://doi.org/10.1016/j.psep.2025.107123.
[9] Y. Zhao, X. Zhou, Q. Zhou, F. Cheng, W. Guo, Solid waste binder cemented dihydrate phosphogypsum aggregate to prepare backfill material, Miner. Eng. 226 (2025) 109249, https://doi.org/10.1016/j.mineng.2025.109249.
[10] Z.G. Fu, D.P. Qiao, Z.L. Guo, K.G. Li, J.C. Xie, J.X. Wang, A model for calculating strength of ultra-fine tailings cemented hydraulic fill and its application, Rock. Soil Mech. 39 (9) (2018) 3147–3156, https://doi.org/10.16285/j.rsm.2017.1510 (In Chinese With English Abstract).
[11] Y.Z. Rao, Mechanism study and experiment of Fly ash used for tail sand cement filling, J. South. Inst. Metall. 24 (2) (2003) 1–5, https://doi.org/10.3969/j.issn.2095-3046.2003.02.001 (In Chinese With English Abstract).
[12] H. Li, A. Jin, S. Chen, Y. Zhao, Mechanical properties and microstructure of coal cinder-based ultra-fine tailings cemented tailings body, Case Stud. Constr. Mater. 20 (2024) e02763, https://doi.org/10.1016/j.cscm.2023.e02763.
[13] L. Zou, J. Xing, J. Xiang, Y. Zhao, Q. Zhang, J. Qiu, Mechanical behavior and microscopic mechanism of synergistically enhanced cemented ultra-fine tailings backfill with polypropylene fiber and silica fume, Constr. Build. Mater. 443 (2024) 137668, https://doi.org/10.1016/j.conbuildmat.2024.137668.
[14] Y. Tian, S.C. Wu, J.J. Li, K.K. Sun, Optimization of mix ratio of Alkali-Activated Slag-Fly ash mortar based on response surface methodology, Bull. Chin. Ceram. Soc. 43 (11) (2024) 4177–4184 (In Chinese With English Abstract).
[15] Y.H. Yang, M. Zheng, S. Yuan, G.T. Zhang, H.Y. Yu, L.Q. Zhang, Study on mix proportion optimization and durability of concrete prepared from mining and metallurgical solid waste, Nonferrous Met. (Mine Sect.) 76 (5) (2024) 185–192, https://doi.org/10.3969/j.issn.1671-4172.2024.05.023 (In Chinese With English Abstract).
[16] Y.F. Hu, K.Q. Li, B. Han, L.J. Zheng, Y.Y. Fan, K. Ji, Influence and mix proportion optimization of composite cementation system on strength of wet shotcrete with tailings, J. Cent. South Univ. (Sci. Technol.) 52 (11) (2021) 3999–4009, https://doi.org/10.11817/j.issn.1672-7207.2021.11.021.
[17] D.C. Wen, D.B. Wei, L.D. Wu, G.B. Ren, H.Z. Guo, Research on mix design and characteristics of UHPC matrix mixture based on MAA model, J. Build. Mater. 25 (7) (2022) 693–699, https://doi.org/10.3969/j.issn.1007?9629.2022.07.006 (In Chinese With English Abstract).
[18] Y. Hu, K. Li, B. Zhang, B. Han, Strength investigation and prediction of superfine tailings cemented paste backfill based on experiments and intelligent methods, Materials 16 (11) (2023), https://doi.org/10.3390/ma16113995.
[19] A.E. Osemudiamhen, L. Ma, I. Ngo, G. Cao, Machine learning-driven strength prediction for solid waste-based backfill materials using infrared radiation indices, Infrared Phys. Technol. 149 (2025), https://doi.org/10.1016/j.infrared.2025.105898.
[20] M. Jooshaki, A. Nad, S. Michaux, A systematic review on the application of machine learning in exploiting mineralogical data in mining and mineral industry, Minerals 11 (8) (2021), https://doi.org/10.3390/min11080816.
[21] S.Q. Liu, L. Liu, E. Kozan, P. Corry, M. Masoud, S. Chung, X. Li, Machine learning for open-pit mining: a systematic review, Int. J. Min. Reclam. Environ. 39 (1) (2025) 1–39, https://doi.org/10.1080/17480930.2024.2362579.
[22] K.S. Shah, H.U. Rehman, N.M. Shahani, B. Ullah, N. Abbas, M. Junaid, M.H.B.M. Hashim, Towards safer mining environments: an in-depth review of predictive models for accidents, Arab. J. Geosci. 17 (11) (2024) 292, https://doi.org/10.1007/s12517-024-12090-4.
[23] S. Indhumathi, S. Praveen Kumar, M. Pichumani, Reconnoitring principles and practice of modified andreasen and andersen particle packing theory to augment engineered cementitious composite, Constr. Build. Mater. 353 (2022) 129106, https://doi.org/10.1016/j.conbuildmat.2022.129106.
[24] W. Zhang, M. Zheng, L. Zhu, Y. Lv, Mix design and characteristics evaluation of high-performance concrete with full aeolian sand based on the packing density theory, Constr. Build. Mater. 349 (2022) 128814, https://doi.org/10.1016/j.conbuildmat.2022.128814.
[25] Z. Hu, R. Liu, K. Li, Z. Wang, K. Gu, W. He, Performance analysis and design optimization of a novel trombe wall system using CFD and response surface method, Energy 324 (2025) 136031, https://doi.org/10.1016/j.energy.2025.136031.
[26] W. Long, Z. Xin-xin, Z. Zi-mu, Z. Ting-An, L. Guo-Zhi, D. Zhi-He, L. Yan, F. Zhi-yu, Synergistic recovery for al and ga within high-alumina Fly ash by carbochlorination using the response surface method, Waste Manag. 203 (2025) 114853, https://doi.org/10.1016/j.wasman.2025.114853.
[27] M. Dafalla, A. Inayat, F. Jamil, C. Ghenai, L. Rocha-Meneses, A. Shanableh, Integrated approach for response surface methodology optimization in biochar and bio-oil production from moringa seeds: pyrolysis enhancement with zeolite catalyst, Bioresour. Technol. Rep. 30 (2025) 102123, https://doi.org/10.1016/j.biteb.2025.102123.
[28] W. Chen, M. Carrera Uribe, E.E. Kwon, K.A. Lin, Y. Park, L. Ding, L.H. Saw, A comprehensive review of thermoelectric generation optimization by statistical approach: taguchi method, analysis of variance (ANOVA), and response surface methodology (RSM), Renew. Sustain. Energy Rev. 169 (2022) 112917, https://doi.org/10.1016/j.rser.2022.112917.
[29] Z. Mahdavi, S.D. Daylami, A. Fadavi, M. Mahfeli, Application of RSM- CCD methodology and image J. For modeling and optimization of orchid protocorm encapsulation, Heliyon 11 (4) (2025) e42744, https://doi.org/10.1016/j.heliyon.2025.e42744.
[30] J. Schindelin, C.T. Rueden, M.C. Hiner, K.W. Eliceiri, The ImageJ ecosystem: an open platform for biomedical image analysis, Mol. Reprod. Dev. 82 (7-8) (2015) 518–529, https://doi.org/10.1002/mrd.22489.
[31] X. Sun, J. Xiang, B. Xiong, X. Kong, J. Qiu, Combined biological and cement solidification of lead-zinc tailings for backfill preparation and its environmental effects, Constr. Build. Mater. 420 (2024) 135601, https://doi.org/10.1016/j.conbuildmat.2024.135601.
[32] Y. Sun, Y. Zhao, X. Wan, J. Qiu, P. Wu, X. Sun, Stabilization/solidification of lead- and cadmium-containing tailings for cemented paste backfill by using clinker-free binders, Constr. Build. Mater. 359 (2022) 129469, https://doi.org/10.1016/j.conbuildmat.2022.129469.
[33] T. Zhao, H. Yang, S. Zhang, Z. Wu, The promoting effect of fe on the immobilization of heavy metals in MSWI FA–lead–zinc tailings-based backfill materials under field application: dynamic simulation leaching and immobilization mechanisms, Chem. Eng. J. 498 (2024) 155734, https://doi.org/10.1016/j.cej.2024.155734.
[34] T. Zhao, S. Zhang, H. Yang, W. Ni, J. Li, G. Zhang, G. Teng, X. Li, S. Guo, Y. Zhou, Z. Wu, Leaching and hydrating mechanisms, economic benefits of backfill materials by using coal Fly ash–slag-based binder for environmentally sustainable production, Constr. Build. Mater. 397 (2023) 132360, https://doi.org/10.1016/j.conbuildmat.2023.132360.
[35] T. Zhao, S. Zhang, H. Yang, Q. Sun, Z. Wu, G. Li, B. Zhang, W. Ni, The effect of chlorine content on the performance of washed MSWI FA-bottom ash-slag-based binders: hydration mechanism and thermal/kinetic characteristics, Process Saf. Environ. 197 (2025) 106967, https://doi.org/10.1016/j.psep.2025.106967.
[36] C. Lin, H. Zhang, C. Wang, C. Chen, Z. Li, J. Zhang, Q. Li, W. Ma, Study on the mechanical properties and solidification mechanism of ground granulated blast furnace slag-carbide slag-desulfurization gypsum solidified shield musk, Constr. Build. Mater. 475 (2025) 141166, https://doi.org/10.1016/j.conbuildmat.2025.141166.
[37] Z. Liu, W. Ni, Y. Li, H. Ba, N. Li, Y. Ju, B. Zhao, G. Jia, W. Hu, The mechanism of hydration reaction of granulated blast furnace slag-steel slag-refining slag-desulfurization gypsum-based clinker-free cementitious materials, J. Build. Eng. 44 (2021) 103289, https://doi.org/10.1016/j.jobe.2021.103289.
[38] Y. Wan, W. Liu, X. Liu, C. Li, Z. Zhou, Z. Zhao, H. Li, Fabrication of eco-friendly mine backfill materials using lead smelting-granulated blast furnace slag-based binder and aeolian sand: heavy metal leaching behavior and performance design, Constr. Build. Mater. 483 (2025) 141655, https://doi.org/10.1016/j.conbuildmat.2025.141655.

[39] Y. Luan, J. Wang, T. Ma, S. Wang, C. Li, Modification mechanism of flue gas desulfurization gypsum on Fly ash and ground granulated blast-furnace slag alkali-activated materials: promoting Green cementitious material, Constr. Build. Mater. 396 (2023) 132400, https://doi.org/10.1016/j.conbuildmat.2023.132400.
[40] S. Seyedian Choubi, C. Meral Akgul, Fixated flue gas desulfurization scrubber sludge-ground granulated blast-furnace slag blends as one-part sustainable binders, Constr. Build. Mater. 462 (2025) 139517, https://doi.org/10.1016/j.conbuildmat.2024.139517.
[41] Y. Feng, B. Tian, Z. Shen, Y. Sun, H. Zhang, L. Xu, L. Gan, R. Wang, A novel inversion approach for seepage parameter of concrete face rockfill dams based on an enhanced sparrow search algorithm, Comput. Geotech. 183 (2025) 107214, https://doi.org/10.1016/j.compgeo.2025.107214.
[42] Y. Deng, D. Tan, X. Shen, Z. Wang, J. Wu, A hybrid approach to network disintegration: integrating graph convolutional network and genetic algorithm, Chaos Solitons Fractals 197 (2025) 116488, https://doi.org/10.1016/j.chaos.2025.116488.
[43] G.H. Ta, M.K. Leong, A novel in silico approach for predicting unbound brain-to-plasma ratio using machine learning-based support vector regression, Comput. Biol. Med. 192 (2025) 110366, https://doi.org/10.1016/j.compbiomed.2025.110366.
[44] Y. Ding, X. He, R. Zhang, H. Wu, Y. Bu, Random forest-assisted Raman spectroscopy and rapid detection of sweeteners, Infrared Phys. Technol. 148 (2025) 105871, https://doi.org/10.1016/j.infrared.2025.105871.
[45] S.G. Kangalli Uyar, B.K. Ozbay, B. Dal, Interpretable building energy performance prediction using XGBoost quantile regression, Energ. Build. 340 (2025) 115815, https://doi.org/10.1016/j.enbuild.2025.115815.
[46] K. Zhu, S. Zhao, X. Luan, F. Liu, Optimal modeling of fermentation process using hybrid support vector regression, J. Process Control 150 (2025) 103429, https://doi.org/10.1016/j.jprocont.2025.103429.
[47] F. Liu, L. Qiao, H. Sang, X. Sun, F. Huang, A self-adaptive particle swarm speed optimization method for unmanned sailboats considering roll constraint, Ocean Eng. 331 (2025) 121365, https://doi.org/10.1016/j.oceaneng.2025.121365.
[48] W. Jiang, Z. Liu, Y. Wang, Y. Lin, Y. Li, F. Bi, Enhancing jamming source tracking capability via adaptive grey wolf optimization mechanism for passive radar network, Signal Process 235 (2025) 110026, https://doi.org/10.1016/j.sigpro.2025.110026.
[49] B. Zhang, K. Li, S. Zhang, Y. Hu, B. Han, Strength prediction and application of cemented paste backfill based on machine learning and strength correction, Heliyon 8 (8) (2022) e10338, https://doi.org/10.1016/j.heliyon.2022.e10338.

Further reading

[1] L. Jia, L. Jiang, Y. Wen, J. Wu, H. Wang, Performance prediction and sensitivity analysis of tunnel boring machine in various geological conditions using an ensemble extreme learning machine, Autom. Constr. 175 (2025) 106169, https://doi.org/10.1016/j.autcon.2025.106169.
[2] Y. Wang, Q. Kong, J. Gao, S. Chen, Research on on-line detection of CO and CO2 mixed gas concentration based on improved extreme learning machine and TDLAS, Infrared Phys. Technol. 148 (2025) 105868, https://doi.org/10.1016/j.infrared.2025.105868.